

# A symmetry-protected topological optical lattice clock

Tianrui Xu,<sup>1,2,3</sup> Anjun Chu,<sup>1,2</sup> Kyungtae Kim,<sup>1</sup> James K. Thompson,<sup>1</sup> Jun Ye,<sup>1</sup> Tilman Esslinger,<sup>4</sup> and Ana Maria Rey<sup>1,2</sup>

<sup>1</sup>*JILA, NIST and Department of Physics, University of Colorado, Boulder, Colorado 80309, USA*

<sup>2</sup>*Center for Theory of Quantum Matter, University of Colorado, Boulder, Colorado 80309, USA*

<sup>3</sup>*Institut Quantique and Département de Physique,*

*Université de Sherbrooke, Sherbrooke, Québec J1K 2R1, Canada*

<sup>4</sup>*Institute for Quantum Electronics & Quantum Center, ETH Zurich, 8093 Zurich, Switzerland*

We theoretically propose a tunable implementation of symmetry-protected topological phases in a synthetic superlattice, taking advantage of the long coherence time and exquisite spectral resolutions offered by gravity-tilted optical lattice clocks. We describe a protocol similar to Rabi spectroscopy that can be used to probe the distinct topological properties of our system. We then demonstrate how the sensitivity of clocks and interferometers can be improved by the topological robustness to unwanted experimental imperfections. The proposed implementation opens a path to exploit the unique opportunities offered by symmetry-protected topological phases in state-of-the-art quantum sensors.

## I. INTRODUCTION

Recent years have witnessed rapid and exciting new developments of optical lattice clocks (OLCs) with excellent quantum coherence and exquisite spectral resolutions<sup>1–10</sup>. Such platforms are ideal for quantum sensing, and have recently reached clock measurement precision at  $7.6 \times 10^{-21}$  and near minute-long atomic coherence<sup>6,10</sup>, making it possible to precisely measure quantities of small magnitudes, such as the gravitational redshift across a millimeter- to centimeter-length scale<sup>6,7</sup>.

In parallel, over the past decades, the rapid development of quantum simulation with cold atomic systems has enabled experimental investigations of topological properties of quantum matter.<sup>11</sup> In particular, significant progress has been made to experimentally realize a class of topological states of matter, referred to as “symmetry-protected topological (SPT) phases.” This type of quantum matter has the property of being insulating in the bulk (i.e., having a gapped dispersion) while conducting at the boundary (i.e., having a gapless dispersion) as long as a certain global symmetry is preserved. Namely, the SPT phases are robust to perturbations that respect said global symmetry and do not close the bulk gap. A prototypical model of a symmetry-protected topological system is the celebrated Su-Schrieffer-Heeger (SSH) model<sup>12,13</sup>. This model, and its closely related models such as the Rice-Mele (RM) model<sup>14</sup>, have been realized in a variety of settings including superlattices<sup>15–18</sup>, momentum-space lattices<sup>19–21</sup>, Rydberg atoms<sup>22</sup> and multilevel systems<sup>23</sup>. Many interesting properties and dynamics of the SSH/RM model have been observed in these experiments, such as soliton/edge state dynamics<sup>19,22,24,25</sup>, Zak phase<sup>15,20,26</sup>, Thouless pumping<sup>16–18,27</sup>, edge-to-edge transport<sup>21</sup> and topological quantum walks<sup>20</sup>.

At the moment, however, quantum simulations of topological quantum matter appear to be independent from the field of quantum sensing. While the realization

of topological phases is exciting in its own right, what is even more appealing is the potential use of topological robustness to remove vulnerability of sensors to unwanted noise while keeping their sensitivity to the desired signal. Achieving this goal requires one to first realize topological phases in state-of-the-art quantum sensors, then to explore the metrological benefits, if any, gained from the underlying topological robustness.

In this manuscript, we discuss a protocol to create a symmetry-protected, topologically non-trivial model in a tilted one-dimensional (1D) OLC. The tilt can come from the gravity by positioning the OLC vertically<sup>6,8</sup>, or by accelerating the OLC along a direction that is not perpendicular to it<sup>7</sup>. In this regime, the atomic wavefunction spatially delocalizes across several lattice sites, allowing us to tunably drive tunneling between different lattice sites, thus creating a SPT system. Then, we discuss how the topological robustness of this system can help suppress the sensitivity of the system to undesirable noise sources, thus improving the performance of OLCs, not only as clocks but also as matter-wave interferometers<sup>28</sup>. Specifically, we first discuss a protocol to engineer the SSH model with tunable model parameters in OLCs. Secondly, we discuss how to probe and characterize the different topological phases of the SSH model using clock spectroscopy. Finally, we discuss how topology protects the system’s sensitivity against unwanted noise in quantum sensing protocols of (1) the optical transition frequency and (2) the local gravitational potential. Our work can be readily implemented in current experimental platforms<sup>8,10</sup>, and paves ways to study topological phases of quantum matter in OLCs. More importantly, our work opens up a path to use topological protection for clock operations.

## II. THE SU-SCHRIEFFER-HEEGER MODEL IN A TILTED OLC

In this section, we discuss our proposal to simulate the SSH/RM model, which is the prototypical model featuring symmetry protected topological phases, in a 1D tilted OLC. We then briefly review the key concepts of this model relevant for the rest of this manuscript.

We consider a tilted, 1D OLC with lattice spacing  $a_L$  and nearest-neighbor tunneling frequency  $J$ , loaded with a dilute array of atoms in such a way the system can be considered as non-interacting, as shown in Fig. 1-(a). The atoms have mass  $M_a$ , and experience a uniform acceleration  $g_{acc}$  generated by a linear potential across the lattice. The eigenstates of this system are the Wannier-Stark (WS) states,  $|l\rangle$ <sup>8,29</sup>, centered at lattice site  $l$  and with eigenenergy  $E_l = \hbar\Delta l$ , where  $\hbar\Delta \equiv M_a g_{acc} a_L$  is the energy difference between atoms on adjacent lattice sites. We consider a parameter regime where the lattice depth is shallow enough that  $J$  is comparable to  $\Delta$ , thus  $|l\rangle$  is delocalized across several lattice sites. We show the WS states as shaded areas in the left panel of Fig. 1-(a). The clock states correspond to two electronic levels,  $e$  and  $g$ , with an optical transition frequency  $\omega_a$ . The single-particle Hamiltonian of our system thus reads:

$$\hat{H}_{\text{lab}}^{\text{1P}} = \hbar\Delta \sum_{l,\alpha=g,e} l \hat{c}_{l\alpha}^\dagger \hat{c}_{l\alpha} + \sum_l \hbar\omega_a \hat{c}_{le}^\dagger \hat{c}_{le}, \quad (1)$$

where  $\hat{c}_{l\alpha}$  annihilates a fermionic particle in WS state  $|l\rangle$  and electronic level  $\alpha = g, e$ .

We use a clock laser with wavelength  $\lambda_c$ , propagating along the lattice direction, to drive the ultranarrow clock transition  $g - e$ . When  $\lambda_c/a_L$  is not an integer value, the clock laser imprints a differential phase  $\phi = k_c a_L$  across adjacent lattice sites which generates the spin-orbit coupling (SOC)<sup>30-33</sup>, allowing the clock laser to drive  $g - e$  transitions between different sites. We propose to use two different clock laser tones to implement the SSH/RM model. The first tone with angular frequency  $\omega_0$ , detuned from the atomic transition by  $\delta = \omega_0 - \omega_a$ , drives the on-site (“carrier”,  $|l, g\rangle \rightarrow |l, e\rangle$ ) transition (see Fig. 1-(a) and Appendix. A for details):

$$\hat{H}_{\text{lab}}^{\tilde{\Omega}_0} = \frac{\hbar\tilde{\Omega}_0}{2} e^{-i\omega_0 t} \sum_l \hat{c}_{le}^\dagger \hat{c}_{lg} + \text{h.c.}, \quad (2)$$

where  $\tilde{\Omega}_0 = \Omega^c \langle l | e^{ik_c \hat{x}} | l \rangle \simeq \Omega^c I_0 \mathcal{J}_0(\tilde{J})$  with  $\Omega^c$  the bare Rabi frequency of the carrier drive and  $I_0 = \int dx e^{ikx} w_0^2(x)$  the on-site overlapping integral of the localized ground-band Wannier function  $w_0(x)$ , and  $\mathcal{J}_n(\tilde{J})$  the  $n$ -th Bessel function of the first kind with  $\tilde{J} = 4J |\sin(\phi/2)| / \Delta$ . The second tone with angular frequency  $\omega_1 = \omega_a + \delta_0 + \delta_t - \Delta$ , is used to drive a “red sideband” transition,  $|l, g\rangle \rightarrow |l-1, e\rangle$ . This tone has a two-photon detuning  $\omega_1 - \omega_0 = \delta_t - \Delta$  and the Hamiltonian reads (see Fig. 1-(a) and Appendix. A for more

details):

$$\hat{H}_{\text{lab}}^{\tilde{\Omega}_1} = \frac{\hbar\tilde{\Omega}_1}{2} e^{-i\omega_1 t} \sum_l \hat{c}_{le}^\dagger \hat{c}_{l+1g} + \text{h.c.}, \quad (3)$$

where  $\tilde{\Omega}_1 = \Omega^s \langle l-1 | e^{ik_c \hat{x}} | l \rangle \simeq i\Omega^s I_0 \mathcal{J}_{-1}(\tilde{J})$  and  $\Omega^s$  is the bare Rabi frequency of the sideband drive. In the above equations, we removed the SOC phase via a gauge transformation:  $\hat{c}_{le} \rightarrow e^{il\phi} \hat{c}_{le}$ . When driving close to resonance of both transitions, it is convenient to go to a rotating-gauge frame (RGF) via

$$\hat{c}_{le}^\dagger \rightarrow \mathbf{i}^l e^{it[(\omega_0 - \omega_1)l + \omega_0]} \hat{a}_{le}^\dagger, \quad \hat{c}_{lg} \rightarrow \mathbf{i}^l e^{it(\omega_0 - \omega_1)l} \hat{a}_{lg}^\dagger, \quad (4)$$

and obtain a tilted RM (t-RM) model:

$$\hat{H}_{\text{t-RM}}/\hbar = \hat{H}_{\text{RM}}/\hbar + \delta_t \sum_{l,\alpha=e/g} l \hat{a}_{l\alpha}^\dagger \hat{a}_{l\alpha}, \quad (5)$$

where

$$\begin{aligned} \hat{H}_{\text{RM}}/\hbar = & \sum_l \left( \frac{\Omega_A}{2} \hat{a}_{le}^\dagger \hat{a}_{lg} + \frac{\Omega_B}{2} \hat{a}_{le}^\dagger \hat{a}_{l+1g} + \text{h.c.} \right) \\ & + \frac{\delta}{2} \sum_l \left( \hat{a}_{lg}^\dagger \hat{a}_{lg} - \hat{a}_{le}^\dagger \hat{a}_{le} \right), \end{aligned} \quad (6)$$

with  $\Omega_A = \tilde{\Omega}_0$ ,  $\Omega_B = -i\tilde{\Omega}_1 \in \mathbb{R}$ . When both drives are on resonance ( $\delta = \delta_t = 0$ ), the t-RM model becomes the SSH model:  $\hat{H}_{\text{SSH}}/\hbar = \sum_l \left( \frac{\Omega_A}{2} \hat{a}_{le}^\dagger \hat{a}_{lg} + \frac{\Omega_B}{2} \hat{a}_{le}^\dagger \hat{a}_{l+1g} + \text{h.c.} \right)$ .

A schematic visualization is shown in Fig. 1-(a). All of the model parameters, namely,  $\Omega_A$ ,  $\Omega_B$ ,  $\delta$  and  $\delta_t$  can be tuned:  $\delta$  and  $\delta_t$  can be tuned via tuning laser frequencies as long as they are smaller than  $\Delta$ ;  $\Omega_A$  and  $\Omega_B$  can be tuned either by tuning the laser Rabi frequencies  $\Omega^c$  and  $\Omega^s$ , the lattice depth (which modifies  $I_0$  and  $J$ ), the spin-orbit coupling phase  $\phi$ <sup>34</sup>, or the tilting potential  $\hbar\Delta$ <sup>7</sup>.

The SSH/RM model has two dimerized phases determined by  $r \equiv \Omega_B/\Omega_A$ . The transition between them is at  $r = 1$ , which sets the topological critical point for the SSH model. When  $r < 1$ , the SSH model is in the topologically trivial (T) phase, while when  $r > 1$ , the topologically non-trivial (NT) phase. One way to visualize these two phases is by rewriting the model in the quasi-momentum ( $k$ ) basis:  $\hat{a}_{k\alpha} = \frac{1}{\sqrt{L}} \sum_l e^{ilk a_L} \hat{a}_{l\alpha}$ , which can then be used to define spin operators acting in quasi-momentum space,  $\hat{S}_k^+ = \hat{a}_{ke}^\dagger \hat{a}_{kg}$  and  $\hat{S}_k^z = (\hat{a}_{ke}^\dagger \hat{a}_{ke} - \hat{a}_{kg}^\dagger \hat{a}_{kg})/2$ . The spin operators satisfy standard commutation relations. In this way,  $\hat{H}_{\text{SSH}}$  can be written as a spin model

$$\hat{H}_{\text{SSH}} = \sum_k \vec{B}(k) \cdot \hat{S}_k, \quad (7)$$

where  $\hat{S}_k = (\hat{S}_k^x, \hat{S}_k^y, \hat{S}_k^z)$ , and the effective magnetic field is defined as  $\vec{B}(k) \equiv (\Omega_A + \Omega_B \cos ka_L, \Omega_B \sin ka_L, 0) \equiv$

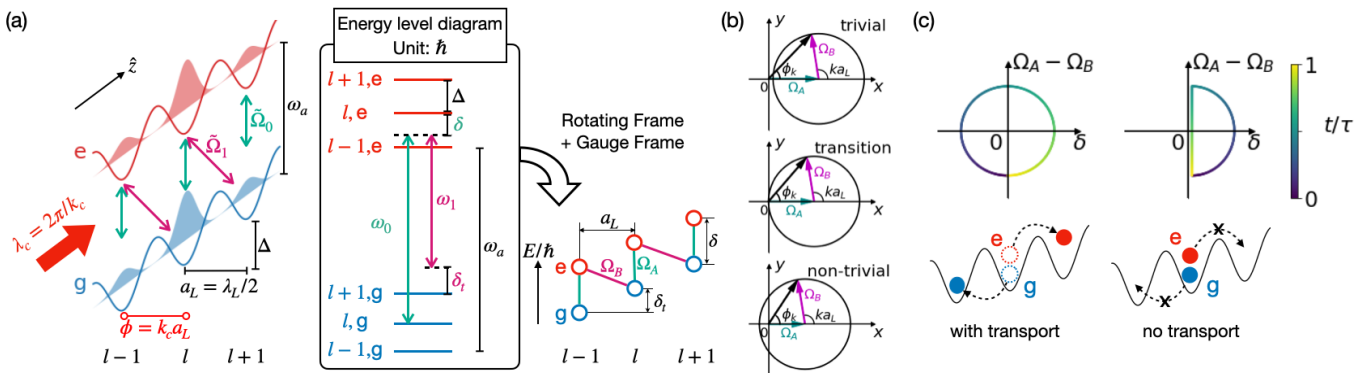


FIG. 1. Simulating the SSH/RM models in a tilted 1D OLC: by using two laser beams to drive both carrier and sideband transitions, a 1D Wannier-Stark ladder can be transformed into the SSH/RM model that we use for quantum simulation and quantum sensing protocols discussed in the rest of the manuscript. (a): Left panel: a schematic diagram of the experimental realization of  $\hat{H}_{\text{t-RM}}$  in a tilted 1D OLC. We use a two-tone clock laser with wavevector  $k_c$  in a tilted 1D OLC with lattice constant  $a_L$ . When the clock laser is incommensurate with the optical lattice, atoms on neighboring lattice sites feel a spin-orbit-coupling phase  $\phi = k_c a_L$ . We show the Wannier-Stark wavefunctions as shaded red and blue areas. Center panel: the energy diagram relevant to generating the SSH model, as indicated in the right panel. (b): Trajectories that  $\vec{B}(k)$  follows when  $k$  is varied over the Brillouin zone in the SSH model, with  $r < 1$  (top),  $r = 1$  (center), and  $r > 1$  (bottom), and their corresponding topological phases. (c): Topological Thouless pumping cycles with (left) and without (right) particle transport, over a time period  $\tau$ . Upper panels: the trajectories in parameter space  $(\delta, \Omega_A - \Omega_B)$ ; lower panels: the corresponding particle transportation, or lack thereof, after one pumping cycle.

$(|B| \cos(\phi_k), |B| \sin(\phi_k), 0)$  with  $\phi_k$  shown in Fig. 1-(b). The topology of the SSH model can thus be seen through a closed trajectory of  $\vec{B}$  along the Brillouin zone (BZ),  $ka_L \in (-\pi, \pi]$ , also shown in Fig. 1-(b). The T/NT phase depends on whether or not this trajectory winds around the origin, as defined by the “winding number”  $\mathcal{W}$  or the Zak phase  $\phi_{\text{Zak}} = -\pi\mathcal{W}$ . Mathematically, for the SSH model,  $\mathcal{W}_{\text{SSH}} = -\frac{1}{\pi} \int_{\text{BZ}} \mathcal{A}(k) dk$  with the Berry phase  $\mathcal{A}(k) = -\frac{1}{2} d\phi_k / dk$ . We thus have  $\mathcal{W}_{\text{SSH}} = 0$  when  $r < 1$  and  $\mathcal{W}_{\text{SSH}} = 1$  when  $r > 1$ .

A non-trivial Berry phase can give rise to topological Thouless pumping<sup>35,36</sup> when one varies the RM model parameters  $(\Omega_A, \Omega_B$  and  $\delta)$  in a way that they adiabatically return to their initial values after a pump cycle time  $\tau$ , as sketched in Fig. 1-(c). The particle transport at the end of each cycle is restricted to be an integer number set by  $\mathcal{W}$  as the trajectory of  $(\delta, \Omega_A - \Omega_B)$  winds around the origin once, otherwise there is no particle transport. The direction towards which the particle moves is determined by its initial state and the winding direction of  $(\delta, \Omega_A - \Omega_B)$ . The topological Thouless pumping is known to be robust against weak perturbations such as interactions and time-independent spatial disorder<sup>36–38</sup>.

### III. A SPECTROSCOPIC PROBE OF THE TOPOLOGICAL PHASE TRANSITION

In the following section, we discuss how we can use standard clock spectroscopy to probe the topological nature of the SPT phases in our system either when  $\delta = \delta_t = 0$ , or when  $\delta_t = 0$  with fixed  $\delta$ .

We use the states  $\{|\downarrow\rangle_l \equiv |l+1, g\rangle, |\uparrow\rangle_l \equiv |l, e\rangle\}$  as an effective two-level system to perform the read out, as done in prior work<sup>6,8</sup>. In terms of these states, we can define the corresponding sideband spin-1/2 operators:  $\hat{I}_l^y \equiv (\hat{a}_{le}^\dagger \hat{a}_{l+1g} - \hat{a}_{l+1g}^\dagger \hat{a}_{le}) / (2i)$ ,  $\hat{I}_l^x \equiv (\hat{a}_{le}^\dagger \hat{a}_{l+1g} + \hat{a}_{l+1g}^\dagger \hat{a}_{le}) / 2$  and  $\hat{I}_l^z \equiv (\hat{a}_{le}^\dagger \hat{a}_{le} - \hat{a}_{l+1g}^\dagger \hat{a}_{l+1g}) / 2$ , which satisfy the appropriate commutation relations. In a typical clock measurement, one measures the *global* observables that is given by the sum of all local observables, namely  $\hat{O} = \sum_l \hat{O}_l$ . We also simplify the expectation value of an operator as  $O = \langle \hat{O} \rangle$ . Additionally, since  $\hat{I}_z$  is the global particle number difference between *e* and *g* state,  $\hat{I}_z = \hat{S}_z \equiv \sum_l (\hat{n}_{le} - \hat{n}_{lg}) / 2$ , where  $\hat{n}_{l,e/g} = \hat{a}_{l,e/g}^\dagger \hat{a}_{l,e/g}$ .

We sketch the schematics of the protocol to measure  $\mathcal{W}_{\text{SSH}}$  in Fig. 2-(a): first, we prepare the atoms in the *g* internal level, each in a Wannier-Stark eigenstate. Similar to Rabi spectroscopy, we illuminate the atoms for time  $t$ . However, in our case, to implement the SSH model, we turn both laser tones on, and drive the carrier and sideband transitions *simultaneously* on resonance, namely,  $\delta = \delta_t = 0$ . At the end of the time evolution, instead of measuring the excitation fraction directly, we need to measure the total sideband coherence,  $I_y$ , along a quadrature perpendicular to the already applied sideband tone. The latter can be measured by suddenly turning off the carrier drive while keeping the sideband drive on, for the specific time required to drive a sideband  $\pi/2$ -pulse,  $U_{\text{RGF}}^{m_1} = \exp[-i\frac{\pi}{2} (\sum_l \hat{I}_l^x)]$ , followed by measuring total excited and ground state populations  $n_{e/g} \equiv \langle \hat{n}_{e/g} \rangle = \sum_l \langle \hat{n}_{l,e/g} \rangle$ , and thus obtain  $S_z$ .

By measuring the sideband coherence  $I_y$ , we can in

fact measure the current of the SSH model given by the rate of change of the wavefunction displacement:

$$\frac{\dot{\hat{x}}}{a_L} = \Omega_B \hat{I}_y, \quad (8)$$

where the displacement is given by  $\hat{x} = a_L \sum_l l(\hat{n}_{le} + \hat{n}_{lg})$ . A similar protocol was performed in quantum gas microscopes to measure currents with single-site resolution<sup>39</sup>.

To probe the topological phase transition, one has to repeat this protocol and measure  $I_y(t)$  at different time  $t$  to obtain its time integral. When weighted by  $\Omega_B$ , we obtain the displacement of the atomic wavefunction from its initial location,  $x(T)$ :

$$\frac{x(T)}{a_L} = \Omega_B \int_0^T dt I_y(t). \quad (9)$$

We show in Fig. 2-(b) that  $x(T)$  can be used to probe topological phases of the SSH model, i.e.,

$$\frac{x(T)}{a_L} = \frac{\mathcal{W}_{\text{SSH}}}{2} + \text{oscillating terms}. \quad (10)$$

In fact, the quantity  $x(T)$  is equivalent to the ‘‘mean displacement’’ (MD), a bulk observable that can be used as a marker of topological phases<sup>40–42</sup>. The MD has been used to measure winding numbers in twisted photons<sup>41</sup>, and can be used to study the topological properties of more complicated models<sup>42</sup>.

The simple limiting cases when the system is totally dimerized, with  $\Omega_B \neq 0$ ,  $\Omega_A = 0$  and  $\Omega_A \neq 0$ ,  $\Omega_B = 0$ , can serve to illustrate the distinct behaviors in the two different topological phases. In the former case, or the topologically non-trivial phase, the atom performs standard Rabi oscillations in the sideband transition  $I_y(t) = \sin(\Omega_B t)/2$  and therefore  $x(T)/a_L = (1 - \cos(\Omega_B T))/2$ ; while in the latter case, or the topologically trivial phase, only the carrier transition is driven, thus atoms remain localized at their initial sites and thus  $I_y(t) = x(T) = 0$ .

In the presence of a small detuning from the carrier transition  $\delta$ , we can measure the MD in *one step*, without integrating over time, by measuring the  $x$ -component of the sideband coherence  $I_x$  after time evolution. We measure  $I_x$  by suddenly applying a phase jump of  $-\pi/2$  on the Rabi sideband drive while simultaneously turning off the carrier Rabi drive, for a time necessary to realize a  $\pi/2$ -pulse,  $U_{\text{RGF}}^{m_2} = \exp\left[\mathbf{i}\frac{\pi}{2}\left(\sum_l \hat{I}_l^y\right)\right]$ , followed by a measurement of the excited/ground state populations  $n_{e,g}$ . We display the above protocol in Fig. 2-(c). One can show analytically using linear responses that when  $\delta_t, \delta \ll \Omega_A, \Omega_B$  (see Appendix. C for details),

$$I_x(t) \simeq \frac{\delta}{\Omega_B} \frac{\mathcal{W}_{\text{SSH}}}{2} + \delta_t \tilde{S}(\Omega_A, \Omega_B) + \text{osc. terms}, \quad (11)$$

where  $\tilde{S}(\Omega_A, \Omega_B)$  is a real-valued function not directly related to  $\mathcal{W}_{\text{SSH}}$  (see Appendix. C and Fig. C.1 for detail). The above equation illustrates that the kinetic

term  $I_x$ <sup>39</sup> responds linearly to the inversion-symmetry-breaking terms  $\delta$  and  $\delta_t$ , with a slope related to  $\mathcal{W}_{\text{SSH}}$  for the carrier detuning  $\delta$ . Again, in the simple limiting case when the system is fully dimerized, we see that  $I_x(t) = 0$  when  $\Omega_A \neq 0$ ,  $\Omega_B = 0$ , while  $I_x(t) \simeq (\delta + \delta_t)(1 - \cos(\Omega_B t))/2$  when  $\Omega_A = 0$ ,  $\Omega_B \neq 0$ .

We show the numerical simulations of  $I_x(t)$  with  $\delta_t = 0$ , at  $t = \pi/\Omega_B$  and  $t = 15\pi/\Omega_B$  in Fig. 2-(d). This provides us a one-step measurement of  $\mathcal{W}_{\text{SSH}}$ : as long as we know the values of  $\Omega_B$  and  $\delta$ , we can measure  $\mathcal{W}_{\text{SSH}}$  via  $I_x$ . We would like to note that  $I_x$  is in fact a band correlation function discussed in prior work<sup>43</sup>.

#### IV. SSH CLOCK SPECTROSCOPY

We now discuss a clock spectroscopy protocol with topologically-reduced sensitivity against unwanted noise in laser parameters, focusing on time-independent amplitude noise.

In conventional Rabi spectroscopy, the atomic frequency is inferred via the so called Rabi lineshape, obtained by first driving a carrier laser  $\Omega_R t_\pi^R = \pi$ -pulse, with a carrier laser detuned from the clock transition frequency by a detuning  $\delta_L = \omega_0 - \omega_a$ , followed by measurements of the populations  $n_e, n_g$  as a function of  $\delta_L$ . The resonance value  $\omega_a = \omega_0$  given by the solution of  $(n_e^{-1}(\delta_c) + n_e^{-1}(\delta'_c))/2 = \delta_{\text{resonance}} = 0$ , typically by choosing  $\delta_c$  and  $\delta'_c$  at the positive and negative slopes of the Rabi line shape at half maximum (FWHM), namely, where the line shape achieves maximum positive and negative slopes. One key issue of this protocol arises from uncertainties of  $\Omega_R$  caused by laser amplitude noise: the deviation of  $\Omega_R$  from its expected value leads to an uncertainty of  $t_\pi^R$  that induces a systematic error of the inferred resonant detuning at the FWHM.

Our SSH clock spectroscopy adopts a similar idea as the Rabi spectroscopy, but we determine  $\omega_a$  using the winding number measurement protocol,  $I_x$ , as discussed in Section. III and Fig. 2-(c),(d). Specifically, we operate in the NT phase by setting  $\Omega_B > \Omega_A$ , let the system evolve for a fixed time  $t_\pi^B = \pi/\Omega_B$ , then measure  $I_x$ .

In addition to the carrier detuning, however, in our symmetry-protected SSH clock, there is also the two-photon detuning  $\delta_t - \Delta$ . In Fig. 3-(a) we show that  $S_z$  varies linearly with respect to  $\delta$  and  $\delta_t$ , as discussed in Eq. 11. The relevant bare parameters,  $\omega_a$  and  $\Delta$ , are inferred by finding a set of detunings that satisfy  $I_x(\delta, \delta_t) + I_x(-\delta, -\delta_t) = 0$ .

In the NT phase, when measuring the carrier detuning  $\delta$ , topology helps to reduce the measurement sensitivity to shot-to-shot, static noise arising from uncertainties in the amplitude and phase of Rabi frequencies  $|\epsilon^\alpha|, |\epsilon^\phi| \ll 1$ , which we model as dimensionless, zero-mean Gaussian random variables with standard deviation  $\sigma^\alpha$  and  $\sigma^\phi\pi$ . The Rabi frequencies thus become  $\Omega_{A/B} = \bar{\Omega}_{A/B} e^{i\epsilon^\phi} (1 + \epsilon^\alpha)$ , where  $\bar{\Omega}_{A/B}$  is the ideal value. We also assume that fluctuations in  $\delta_t$  from its ideal

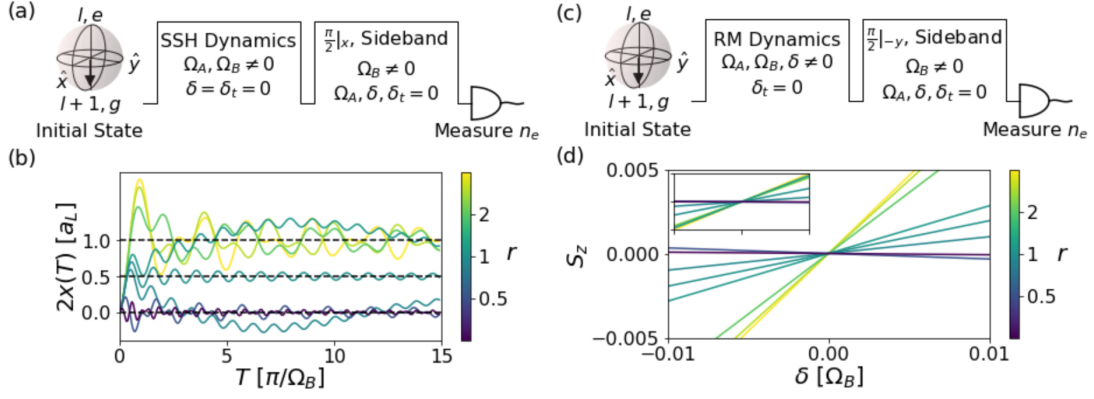


FIG. 2. Probing topological phases in the SSH model. (a)(c): Protocols in the rotating-gauge frame. (b)(d): numerical simulations. (a)(b): Winding number measurements with  $\delta = \delta_t = 0$ , compared to their expected values (0, 0.5 and 1, shown as black horizontal dashed lines) in their corresponding topological phases. Colors of the lines corresponds to different  $r$  values indicated by the colorbar. (c)(d): One-step winding number measurements with  $\delta \neq 0$  and  $\delta_t = 0$ . (d): One-step measurement results as a function of  $\delta/\Omega_B$  at  $\Omega_B t = \pi$  (main panel) and  $\Omega_B t = 15\pi$  (inset). The slope at  $\delta = 0$  gives half of the winding number value. The main panel and the inset share the same  $x$ - and  $y$ -axis, with parameters:  $\delta/\Omega_B = -0.1 \cdots 0.1$ ,  $r = 0.3 \cdots 3$  and  $\delta_t = 0$ .

zero value can be modeled as a zero-mean, Gaussian random number with a standard deviation  $\sigma_t \Omega_B$ . In our simulation, we set  $\sigma^a = 0.01$ ,  $\sigma_\phi = 0.005$ ,  $\sigma_t = 0.001$ ,  $\Omega_B/(2\pi) = 10\text{Hz}$ .

We compare the signals of the Rabi spectroscopy and the SSH spectroscopy at their respective operation points  $\delta_c$ , with  $\Omega_R = \Omega_B$ , and show our numerical results in Fig. 3-(b). We show the median values of the two signals as a function of  $\delta$  near their respective  $\delta_c$  values. We also show as error bars the interval around the median value within which 95.6% of the data lies, indicating the uncertainties of these two signals due to the imperfections discussed in the previous paragraph. The fact that the signal of the SSH spectroscopy has a smaller error bar indicates that it is less affected by the experimental imperfections discussed above.

To quantify the robustness of a measurement protocol against imperfections, we calculate the clock sensitivity to  $\delta$ , assuming a system of  $N$  non-interacting atoms:

$$\Delta^2 \delta = \frac{\langle \Delta^2 \hat{O} \rangle}{t_L^2 (d\langle \hat{O} \rangle / d\varphi)^2}, \quad \langle \Delta^2 \hat{O} \rangle = N/4 + \sigma_s^2, \quad (12)$$

where  $t_L$  is the laser interrogation time,  $\varphi$  is the accumulated phase due to  $\delta$ , and  $\hat{O}$  is the measured observable which gives the signal  $\langle \hat{O} \rangle$ , with variance  $\langle \Delta^2 \hat{O} \rangle$ . The variance includes both the quantum noise, which is  $N/4$  for non-interacting atoms, and the statistical noise  $\sigma_s^2$ , coming from the sensitivity of a protocol to the technical noise. For the collective observable measured in the described protocols,  $\hat{O} = \hat{S}_z$ , the statistical noise increases quadratically in  $N$ <sup>44,45</sup> in the presence of laser amplitude

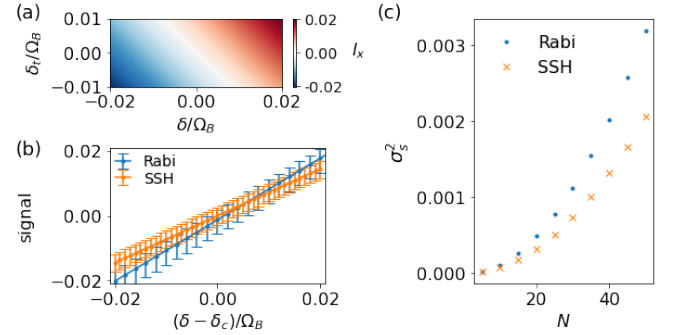


FIG. 3. (a): The signal of the SSH spectroscopy,  $I_x$ , at different  $\delta$  and  $\delta_t$  values without any experimental imperfections. (b) and (c): Comparisons between Rabi spectroscopy (in blue) and SSH spectroscopy (in orange) with  $\Omega_A/(2\pi) = \Omega_B/(4\pi) = 5$  Hz, over 1000 realizations of imperfections. (b): Lines and symbols: median signals ( $(n_e - n_g)/2$  for Rabi and  $I_x$  for SSH) with respect to  $\delta$ , where  $\delta_c$  is the operation point of the measurements:  $\sim 0.8\Omega$  for Rabi spectroscopy and 0 for SSH spectroscopy. Error bars indicate the interval around the median value, within which 95.6% of the data lies. (c):  $N$ -dependence of  $\sigma_s^2$  calculated for the two protocols, where  $N$  is the number of non-interacting particles.

noise, namely,

$$\sigma_s^2 \simeq \sum_{\beta} \sigma_{\Omega_{\beta}}^2 \underbrace{\sum_{i \neq j} \left( \frac{\partial \langle \hat{O}_i \rangle}{\partial \Omega_{\beta}} \Big|_{\Omega_{\beta}} \right) \left( \frac{\partial \langle \hat{O}_j \rangle}{\partial \Omega_{\beta}} \Big|_{\Omega_{\beta}} \right)}_{\propto N^2}, \quad (13)$$

where  $\beta$  is all the Rabi frequencies involved in the protocol, i.e.,  $\beta = R$  for the Rabi spectroscopy and  $\beta = A, B$  for the SSH spectroscopy. In the case of the SSH spectroscopy,  $\sigma_s^2$  is suppressed, as  $I_x \propto \mathcal{W}_{\text{SSH}} \delta$  where  $\mathcal{W}_{\text{SSH}}$

is topologically protected against static amplitude uncertainties of  $\Omega_{A,B}$ <sup>20,43</sup>. We compare  $\sigma_s^2$  values of our protocol with that of the Rabi spectroscopy in Fig. 3-(c) as a function of  $N$ , assuming perfect  $I_x$  measurements. We observe that, despite suffering from an additional noise source from the uncertainty of  $\delta_t$ , the  $N$ -dependence of  $\sigma_s^2$  of the SSH spectroscopy is still smaller than that of the Rabi spectroscopy.

If it is not possible to measure  $I_x$  perfectly, the same quantity can alternatively be measured by first adiabatically preparing an initial state  $(|0, g\rangle + |-1, e\rangle)/\sqrt{2}$ , then turning on the RM dynamics for time  $t^B$ , followed by measuring  $-S_z$ . We show this protocol in Appendix. D. We would like to note that the SSH spectroscopy, just as the Rabi spectroscopy, is expected to be sensitive to the laser phase noise  $\epsilon_\phi$ , as it is the phase we measure in a clock spectroscopy. Additionally, since a non-zero  $\epsilon_\phi$  breaks the time-reversal symmetry, and thus the symmetry of the SSH model, the topology of the SSH model thus cannot protect against it.

## V. TOPOLOGICALLY-PUMPED MATTER-WAVE INTERFEROMETER

Conventional interferometers detect force fields, such as the ones proportional to the local gravitational acceleration  $g$ <sup>46</sup> and the Newtonian gravitational constant  $G$ <sup>47</sup>, via measuring the differential phase,  $\varphi$ , experienced by matterwaves traveling through different paths in the force field. Although state-of-the-art interferometers operate using free falling atoms that enjoy a phase accumulation that scales quadratic in time<sup>48</sup>, trapping the atoms in optical lattices<sup>28,49–53</sup> has the advantage of a much longer interrogation time which is approaching minutes, despite that the phase accumulation rate is limited to scaling linearly with time. A way to further enhance the accumulated phase is via the application of multiple pulses<sup>54,55</sup> that helps to increase the separation between the two parts of the wavepacket.

In a possible implementation of the protocol<sup>55,56</sup>, one first applies an initial carrier  $\pi/2$ -pulse on atoms prepared in their ground state, generating a coherent superposition within a single site  $l$ :  $|\psi_0^{MWI}\rangle = (|l, g\rangle + |l, e\rangle)/\sqrt{2}$ . Then, a sequence of  $N_p^M$  composite  $\pi$ -pulses, consisting of a sideband drive followed by a carrier drive, denoted as  $H_d$ , for a duration  $t_d$ , is applied to induce a spatial separation between  $|e\rangle$  and  $|g\rangle$  states:  $d_{eg} = 2N_p^M a_L$ . Afterwards, within a dark time  $T \gg t_d$ , the state accumulates a differential phase since atoms are in a superposition of states at two separated locations with different gravitational potential. Then, atoms are brought back and recombined using the reversed pulse sequence that separated them, denoted as  $-H_d$ , followed by a measurement of the accumulated phase difference by applying another local carrier  $\pi/2$ -pulse that converts the  $y$ -component of the carrier coherence into population, which is the quantity measured at the end of the

sequence. Assuming fast and perfect  $\pi/2$ -pulses, the total time of this protocol is  $t_f = 2t_d + T$ . This MWI signal depends linearly on the accumulated phase. We refer to this protocol as the “many-pulse” protocol (MPP), and illustrate it in Fig. 4-(a). Assuming perfect drives, the ideal accumulated phase of the MPP is

$$\varphi_{\text{ideal}}^M = \delta_t T d_{eg} / a_L = 2\delta_t (t_f - 2t_d) N_p^M. \quad (14)$$

We now discuss an alternative MWI protocol that shows reduced sensitivity of unwanted noise thanks to the use of topologically-protected adiabatic transfer instead of a multi-pulse sequence. The basic idea is to achieve the desired spatial separation using the topological “Thouless pumping” protocol (TPP), shown in Fig. 4-(b). In this case, within the same time duration  $t_f$ , half of the time is spent to repeat  $N_p^T$  Thouless pumping cycles with a cycle time  $\tau$ , in order to spatially separate the  $|g\rangle$  and  $|e\rangle$  states by  $d_{eg} = 2N_p^T a_L$ . Then, the same amount of time is used to bring the two states back to the initial location, and measure the accumulated phase in the same way as in the MPP. No dark time is needed in this protocol as the two states continuously accumulate differential phases during the adiabatic Thouless pumping cycles. We sketch in the right panel of Fig. 4-(b) the time variation of the RM parameters used to perform a pumping cycle with duration  $\tau = 1/12$  seconds and their corresponding laser frequencies: in the protocol, we change  $\omega_1$  together with  $\omega_0$ , so that the value of  $\delta_t$  is kept at a fixed value at all time. Contrary to the MPP, the ideal accumulated phase scales quadratically with  $t_f$ :

$$\varphi_{\text{ideal}}^T = 4\delta_t \sum_{n=0}^{N_p^T} (n\tau) = 2\delta_t \tau (N_p^T)^2 = \delta_t t_f^2 / (2\tau). \quad (15)$$

We compare MPPs and TPPs with fixed  $t_f = 4$  s and  $\varphi_{\text{ideal}}^M = \varphi_{\text{ideal}}^T$ . In particular, we consider three different MPPs, i.e., protocols  $P_0$  to  $P_2$  with  $P_0$ :  $\Omega/(2\pi) = 24$  Hz,  $N_p^M = 24$ ,  $T = 2$  s;  $P_1$ :  $\Omega/(2\pi) = 40$  Hz,  $N_p^M = 15$ ,  $T = 3.25$  s; and  $P_2$ :  $\Omega/(2\pi) = 40$  Hz,  $N_p^M = 65$ ,  $T = 0.75$  s, adjusting the laser power to achieve the same Rabi frequency  $\Omega$  for both the carrier and the sideband drives. We consider one TPP with  $\tau = 1/12$  s and  $N_p^T = 24$  (protocol  $P_{\text{TPP}}^{\tau=1/12}$  s). All of these protocols have the same ideal phase accumulation.

To investigate the robustness of these protocols, we account for relevant sources of noise, described by the function  $\Omega_{A/B} = \bar{\Omega}_{A/B} (1 + \epsilon^a)$ , where  $\epsilon^a$  is a zero-mean Gaussian variable with standard deviation 0.02. We also take into consideration AC Stark shifts that give rise to an effective carrier detuning  $\sim \Omega_{A/B}^2 \mathcal{J}_{1/0}^2(\tilde{J}) / (4\Delta \mathcal{J}_{0/1}^2(\tilde{J}))$  (See Appendix. E). The TPP is insensitive to the AC Stark shift, as long as the actual path of  $(\delta, \Omega_A - \Omega_B)$ , including the effective detuning, is able to enclose the SSH critical point while keeping adiabaticity.

Both Eq. 14 and Eq. 15 indicate that the accumulated phases of the two protocols depend on (1) the achievable

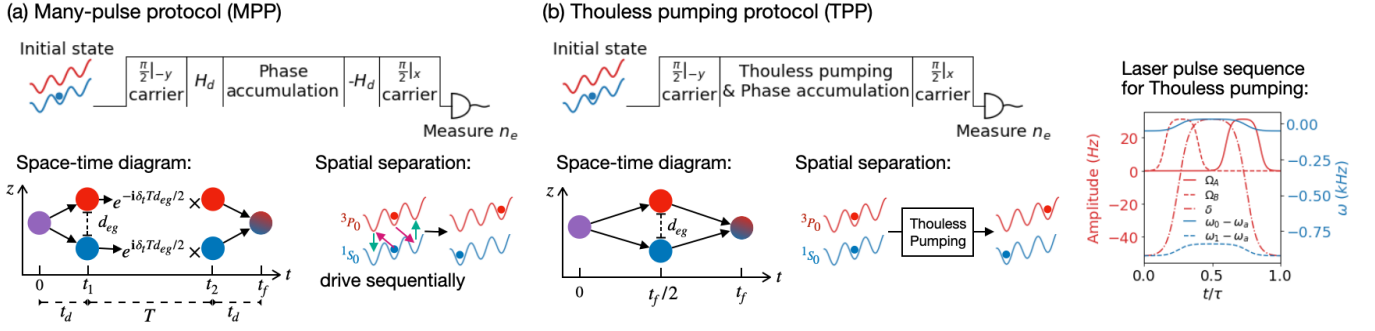


FIG. 4. Matter-wave interferometers (MWIs) in OLCs. (a) The “many-pulse protocol” (MPP). Upper panel: the protocol sequence as described in main text.  $H_d$  denotes the Hamiltonian used to create the spatial separation between  $|g\rangle$  and  $|e\rangle$  states. Lower left panel: the space-time diagram of this interferometer. Lower right panel: pictorial indication of one drive cycle that creates  $d_{eg} = 2a_L$ . (b) The “Thouless pumping protocol” (TPP). Upper left panel: the protocol sequence as described in the main text. Lower left panel: the space-time diagram of this interferometer. Lower center panel: pictorial indication of one drive cycle that creates  $d_{eg} = 2a_L$ . Right panel: laser pulse sequence over one Thouless pumping cycle. In the protocol we change  $\omega_1$  along with  $\omega_0$  so as to keep  $\delta_t$  a fixed value.

spatial separation  $d_{eg}$  and (2) the phase accumulation time. Here, we examine how systematic imperfections affect the achievable spatial separation. It is worth noting that, since we consider an atom in a coherent superposition, due to experimental imperfections, it is no longer the case that  $n_e = n_g = 1/2$  at all times. Therefore, we define the distance between the two states to be:

$$d_{eg} = \frac{x_e}{n_e} - \frac{x_g}{n_g}. \quad (16)$$

Therefore,  $d_{eg}$  is a quantity that implies how fast the differential phase accumulates, *solely* due to the spatial separation of  $e$  and  $g$ .

We show the ratio  $d_{eg}/(2N_p a_L)$  in Fig. 5-(a), where  $2N_p a_L$  is the ideal achievable spatial separation in the absence of imperfections. We observe that TPPs are able to achieve less suppressed  $d_{eg}$  values than the MPPs. We examine the uncertainties via error bars, indicating the interval within which contains 95.6% of the simulated data around its median. Despite being able to achieve larger  $d_{eg}$ , TPPs also appear to have larger uncertainties at large  $N_p$  values, which might arise from the lack of full adiabaticity. To demonstrate this, we show in Fig. 5-(a) a protocol with better adiabaticity by setting  $\tau = 1/5$  s, which we denote as  $P_{\text{TPP}}^{\tau=1/5}$ . This protocol achieves both enhanced  $d_{eg}/(2N_p a_L)$  values and reduced uncertainties. Additionally, the lack of full adiabaticity can also be resolved by optimizing the pulse sequence or via shortcuts-to-adiabaticity protocols<sup>57</sup>. We would like to note that for TPPs, the particle transport is protected even in the presence of small interactions, as long as the interaction strength is small compared to the energy gap of the SSH model.<sup>18,37</sup>

We next compare the time-reversal (TR) process of each of the protocols by studying their “recovery fidelity”  $F$ : assuming  $\delta_t = 0$ , we compute  $F = |\langle \psi(t_f) | \psi_0^{MWI} \rangle|^2$ , namely, the overlap between the particle wave function at the end of the protocol,  $|\psi(t_f)\rangle$ , and the initial state,

$|\psi_0^{MWI}\rangle$ . The recovery fidelity offers a quantitative measure of the robustness of the TR processes of these two protocols. In Fig. 5-(b), we observe that TPP not only has better recovery fidelity (i.e.  $F$  closer to 1), but also has minimal uncertainties as shown by the errorbars, indicating that the TR process of the TPP is less sensitive to systematic imperfections.

Finally, we compare the signal (Fig. 5-(c)) and statistical noise (Fig. 5-(d)) of the protocols. Due to less suppressed  $d_{eg}$  values, the TPP yields faster changes of signals with respect to  $\delta_t$ , as shown by the slope of  $S_y$  in Fig. 5-(c). Moreover, the TPP also yields smaller statistical noise than the MPPs with increasing particle number  $N$ . Therefore, as indicated by Eq. 12, for protocols of the same duration and with the same ideal phase accumulation, the TPP has a better sensitivity than the MPPs.

## VI. CONCLUSION AND OUTLOOK

In this manuscript, we described a readily implementable experimental setting to realize a symmetry-protected topological model in a tilted 1D OLC. We discussed how one can measure the system’s topological properties, namely the winding number, by taking advantage of the pristine quantum coherence and the exquisite spectral resolution offered by OLCs. We finally discussed two sensing protocols which showed improved sensitivity compared to conventional clock sequences thanks to the topological robustness of symmetry-protected states against unwanted global amplitude noise present in real experiments.

Our work can open up a new path for a new generation of OLCs with topologically-enhanced sensitivity. While we focused here on measuring local gravitational acceleration  $g$ , our protocols can, in principle, be adapted to improve the measurement resolution of gravitational red shifts<sup>6</sup>. Moreover, even though so far we have limited

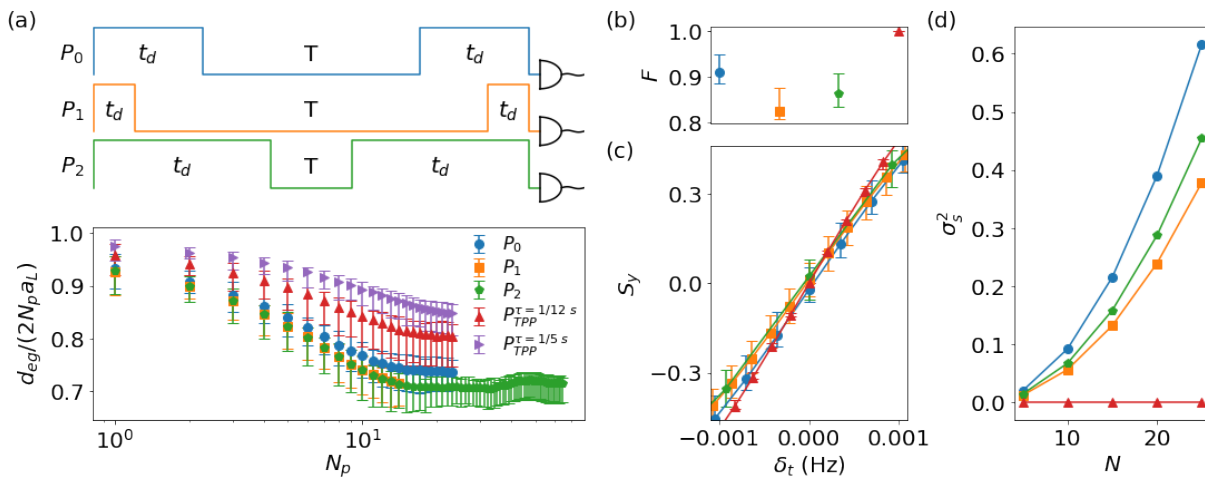


FIG. 5. Comparisons between the MPPs and TPPs for 50 realizations with imperfections as discussed in the main text. The legend of all panels are shown in panel (a). The error bars indicate the range of 95.6% of the data around median. (a): Upper panel: pulse sequences of the MPP protocols  $P_0 \dots 2$ . Lower panel:  $d_{eg}/(2N_p a_L)$  as a function of the number of pumping cycles, where  $2N_p a_L$  is the ideal  $d_{eg}$  values. (b): The recovery fidelity,  $F$ , of the protocols. (c): Signal,  $S_y$ , of the protocols as a function of  $\delta_t$ . (d):  $\sigma_s^2$  calculated as a function of the number of interrogated non-interacting atoms,  $N$ .

our analysis to non-interacting atoms, an exciting extension is to study how interactions affect the observed topological robustness<sup>18,58</sup>. Finally, generalizing the investigation to more complex systems including higher-dimensional models or systems with more than two internal levels, by incorporating the nuclear spins, will open up an plethora of rich physics, where for the first time the cooperation or competition between interactions and topology can give rise to a new generation of quantum enhanced and topologically protected sensors.

## ACKNOWLEDGMENTS

We thank Joanna Lis and Maya Miklos for feedback on the manuscript. We also thank Thomas Bilitewski, Mikhail Mamaev, Klaus Mølmer, Bhuvanesh Sundar, Yanqi Wang and Haoqing Zhang for useful discussions. We additionally thank Jim McKown, Corey Keasling and Daniel Packman from JILA computing group for supports with relevant hardware used for numerical simulations. This material is based upon work supported by the SLOAN, the Simons and the Heising-Simons foundations, the VVFF, the NSF JILA-PFC PHY-2317149 and OMA-2016244 (QLCI), the U.S. Department of Energy, Office of Science, National Quantum Information Science Research Centers, Quantum Systems Accelerator and NIST. TE also acknowledges funding from Swiss National Science Foundation under Advanced grant TMAG-2 209376.

## Appendix A: The SSH Model in a tilted OLC

The Hamiltonian that describes the dynamics of atoms driven by a coherent laser, with Rabi frequency  $\Omega$  and

laser frequency  $\omega_L$ , and wavenumber  $k_L$ , is given by

$$H_{\text{lab}}^\Omega/\hbar = \frac{\Omega}{2} e^{-i\omega_L t} \int dx e^{ik_L x} \hat{\Psi}_e^\dagger(x) \hat{\Psi}_g(x). \quad (\text{A1})$$

Assuming the atoms are trapped in the lowest band of a lattice, we can expand the field operator in term of lowest band Wannier states localized at the different lattice sites, the above equation can be rewritten as  $\hat{\Psi}_\alpha = \sum_n w_0(x - na_l) \hat{c}_{n\alpha}$ , where  $a_l$  is the lattice constant. We thus get

$$\hat{H}_{\text{lab}} = \frac{\Omega}{2} e^{-i\omega_L t} \sum_{mn} I_{nm} \hat{c}_{ne}^\dagger \hat{c}_{mg}, \quad (\text{A2})$$

where

$$I_{nm} = \int dx e^{ik_L x} w_0(x - na_l) w_0(x - ma_l) = e^{in\phi} I_{m-n}, \quad (\text{A3})$$

with  $\phi = ka_L$ . One can prove that  $I_{m-n} = I_n^*$ . If two laser drives are used to illuminate atoms trapped in a tilted system, and  $\delta = m - n$ , the full Hamiltonian describing the motion and internal dynamics of the atoms is given by

$$\begin{aligned} & \hat{H}_{\text{lab}}/\hbar \\ &= \left( \frac{\Omega^c}{2} e^{-i\omega_0 t} \sum_{l\delta} I_\delta e^{il\phi} \hat{c}_{le}^\dagger \hat{c}_{l+\delta g} + \text{h.c.} \right) \\ &+ \left( \frac{\Omega^s}{2} e^{-i\omega_1 t} \sum_{l\delta} I_\delta e^{il\phi} \hat{c}_{le}^\dagger \hat{c}_{l+\delta g} + \text{h.c.} \right) \\ &- J \sum_{l\alpha} \hat{c}_{l+1\alpha}^\dagger c_{l\alpha} + \omega_a \sum_l \hat{c}_{le}^\dagger \hat{c}_{le} + \Delta \sum_{l\alpha} l \hat{c}_{l\alpha}^\dagger \hat{c}_{l\alpha}, \quad (\text{A4}) \end{aligned}$$

where  $\hbar\Delta = Mg_{acc}a_L$  is the the potential energy difference between atoms at adjacent lattice sites. Rewriting



the Hamiltonian in terms of Wannier-Stark (WS) states, that diagonalize the motional degrees of freedom:

$$\hat{H}/\hbar = -J \sum_{l\alpha} \hat{c}_{l+1\alpha}^\dagger \hat{c}_{l\alpha} + \Delta \sum_{l\alpha} l \hat{c}_{l\alpha}^\dagger \hat{c}_{l\alpha} + \text{h.c.},$$

with  $\hat{c}_{l\alpha} = \sum_m \mathcal{J}_{l-m} (2J/\Delta) \hat{c}_{m\alpha}$ , we have<sup>59</sup>

$$\sum_l e^{il\phi} \hat{c}_{le}^\dagger \hat{c}_{l+\delta g} = \sum_{lk} e^{il\phi} e^{-i(\delta-k)(\pi+\phi)/2} \mathcal{J}_{\delta-k}(\tilde{J}) \hat{c}_{le}^\dagger \hat{c}_{l+kg}, \quad (\text{A5})$$

where  $\tilde{J} = 4J |\sin(\phi/2)|/\Delta$ . As a result,  $\hat{H}_{\text{lab}}/\hbar$  becomes:

$$\begin{aligned} & \hat{H}_{\text{lab}}/\hbar \\ &= \frac{\Omega^c}{2} e^{-i\omega_0 t} \sum_{lk\delta} I_\delta e^{il\phi} e^{-i(\delta-k)(\pi+\phi)/2} \mathcal{J}_{\delta-k}(\tilde{J}) \hat{c}_{le}^\dagger \hat{c}_{l+kg} + \text{h.c.} \\ &+ \frac{\Omega^s}{2} e^{-i\omega_1 t} \sum_{lk\delta} I_\delta e^{il\phi} e^{-i(\delta-k)(\pi+\phi)/2} \mathcal{J}_{\delta-k}(\tilde{J}) \hat{c}_{le}^\dagger \hat{c}_{l+kg} + \text{h.c.} \\ &+ \omega_a \sum_l \hat{c}_{le}^\dagger \hat{c}_{le} + \Delta \sum_{l\alpha} \hat{c}_{l\alpha}^\dagger \hat{c}_{l\alpha}. \end{aligned} \quad (\text{A6})$$

Assuming that the lattice is deep enough that the Wannier states are mostly localized at a single lattice site, and that the carrier and sideband Rabi frequencies are weak and thus cannot drive undesirable transitions, we can set  $\delta = 0$  and  $k = 0$ , and ignore other terms (see Appendix. E when the  $k = 0$  approximation is not assumed). In this case we obtain

$$\begin{aligned} & H_{\text{lab}}/\hbar \\ &\simeq \frac{\Omega^c I_0}{2} e^{-i\omega_0 t} \sum_l \left( e^{il\phi} \mathcal{J}_0(\tilde{J}) \hat{c}_{le}^\dagger \hat{c}_{lg} \right. \\ &\quad \left. + e^{il\phi} e^{i(\pi+\phi)/2} \mathcal{J}_{-1}(\tilde{J}) \hat{c}_{le}^\dagger \hat{c}_{l+1g} \right) \\ &+ \frac{\Omega^s I_0}{2} e^{-i\omega_1 t} \sum_l \left( e^{il\phi} \mathcal{J}_0(\tilde{J}) \hat{c}_{le}^\dagger \hat{c}_{lg} \right. \\ &\quad \left. + e^{il\phi} e^{i(\pi+\phi)/2} \mathcal{J}_{-1}(\tilde{J}) \hat{c}_{le}^\dagger \hat{c}_{l+1g} \right) \\ &+ \omega_a \sum_l \hat{c}_{le}^\dagger \hat{c}_{le} + \Delta \sum_{l\alpha} l \hat{c}_{l\alpha}^\dagger \hat{c}_{l\alpha}. \end{aligned} \quad (\text{A7})$$

## Appendix B: Analytical derivation of $x(T)/a_L$ in the SSH model

The SSH model in the quasimomentum space reads:

$$\hat{H}_{\text{SSH}}/\hbar = \sum_k \left( \frac{\Omega_A}{2} \hat{a}_{ke}^\dagger \hat{a}_{kg} + \frac{\Omega_B}{2} e^{-ikaL} \hat{a}_{ke}^\dagger \hat{a}_{kg} + \text{h.c.} \right), \quad (\text{B1})$$

with eigenenergies

$$E_k^\pm = \pm E_k = \pm \frac{1}{2} \sqrt{\Omega_A^2 + \Omega_B^2 + 2\Omega_A \Omega_B \cos kaL}$$

and eigenvectors

$$|k, \pm\rangle = \frac{1}{\sqrt{2}} \left( \pm e^{-i\phi k} \hat{a}_{ke}^\dagger + \hat{a}_{kg}^\dagger \right) |0\rangle, \quad (\text{B2})$$

where

$$\tan \phi_k = \frac{\Omega_B \sin kaL}{\Omega_A + \Omega_B \cos kaL}.$$

The operator  $\hat{I}_y$  and the initial state in k-space are:

$$\hat{I}_y = -\mathbf{i} \sum_k e^{-ikaL} \hat{a}_{ke}^\dagger \hat{a}_{kg} + \text{h.c.} \quad (\text{B3})$$

and

$$\begin{aligned} |\psi_0\rangle &= \hat{a}_{0g}^\dagger |0\rangle = \frac{1}{\sqrt{L}} \sum_k \hat{a}_{kg}^\dagger |0\rangle \\ &= \frac{1}{\sqrt{2L}} \sum_k (|k, +\rangle - |k, -\rangle). \end{aligned} \quad (\text{B4})$$

We thus obtain

$$\begin{aligned} I_y(t) &= -\mathbf{i} \langle 0 | \hat{a}_{kg} e^{iHt} \sum_p e^{-ipaL} \hat{a}_{pe}^\dagger \hat{a}_{pg} e^{-iHt} \hat{a}_{kg}^\dagger | 0 \rangle + \text{c.c} \\ &= \frac{1}{2L} \sum_k \left( \frac{\Omega_A \cos kaL + \Omega_B}{E_k^2} \right) \sin(2E_k t) \end{aligned} \quad (\text{B5})$$

Thus

$$\begin{aligned} \frac{x(T)}{\Omega_B a_L} &= \int_0^T dt I_y(t) \\ &= \frac{1}{2L} \sum_k \left( \frac{\Omega_A \cos kaL + \Omega_B}{E_k^2} \right) [1 - \cos(2E_k T)] \\ &\xrightarrow{L \rightarrow \infty} \frac{a_L}{8\pi} \int_{-\pi}^{\pi} dk \left( \frac{\Omega_A \cos kaL + \Omega_B}{E_k^2} \right) \\ &\quad \times [1 - \cos(2E_k T)] \end{aligned} \quad (\text{B7})$$

We identify the Berry phase from the above equation:

$$\mathcal{A}(k) \equiv -\frac{1}{2} \frac{d\phi_k}{dk} = -\frac{1}{2} \frac{a_L \Omega_B (\Omega_A \cos kaL + \Omega_B)}{4E_k^2}, \quad (\text{B8})$$

and recall the relation between Berry phase and the winding number,  $\mathcal{W}$ :

$$\mathcal{W} = -\frac{1}{\pi} \int_{\text{BZ}} \mathcal{A}(k) dk. \quad (\text{B9})$$

Thus the winding number relates to  $x(T)$  via

$$\frac{x(T)}{a_L} = \frac{\mathcal{W}_{\text{SSH}}}{2} - \frac{1}{2} \int_{\text{BZ}} \frac{dk}{2\pi} \frac{d\phi_k}{dk} \cos(2E_k T). \quad (\text{B10})$$

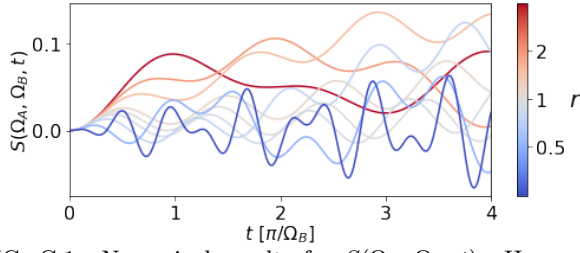


FIG. C.1. Numerical results for  $S(\Omega_A, \Omega_B, t)$ . Here we fix  $\Omega_B/(2\pi) = 10$  Hz and vary  $r$  values.

### Appendix C: $I_x$ in the presence of small $\delta$ , $\delta_t$

We can use linear response theory/perturbation theory to understand the effect of non-zero but small detunings,  $\delta$  and  $\delta_t$ . Using  $\hat{O} = \hat{O}_0 + \Delta\hat{O}$ , where  $\hat{O}_0$  is the unperturbed operator, and

$$\Delta\hat{O} \simeq \mathbf{i} \int_0^t ds \left[ \Delta\hat{H}(s), \hat{O}(t) \right], \quad (\text{C1})$$

where both  $\Delta\hat{H}(s)$  and  $\hat{O}(t)$  are in the Heisenberg picture of  $H_{\text{SSH}}$ . We thus obtain for the case when the unperturbed Hamiltonian is the SSH model:

$$\Delta\hat{I}_x(t) = \mathbf{i} \int_0^t ds \left[ \hat{U}^\dagger(s) \Delta\hat{U}(s), \hat{I}_x(t) \right], \quad (\text{C2})$$

where  $\hat{U}(s) = e^{-\mathbf{i}\hat{H}_{\text{SSH}}s}$ . When  $\Delta\hat{H} = -\delta \sum_l \hat{S}_l^z$ ,

$$\begin{aligned} \Delta\hat{I}_x(t) &= -\mathbf{i}\delta \int_0^t ds \left[ \hat{U}^\dagger(s) \sum_l \hat{S}_l^z \hat{U}(s), \hat{U}^\dagger(t) \hat{I}_x \hat{U}^\dagger(t) \right] \\ &= \frac{\delta}{2L} \sum_k \frac{\cos(2E_k t) - 1}{2E_k} \left[ e^{\mathbf{i}(-ka_L + \phi_k)} + \text{c.c.} \right] \hat{\sigma}_k^z. \end{aligned} \quad (\text{C3})$$

One can evaluate  $\Delta\hat{I}_x(t)$  at the initial condition  $|0\rangle = |0, g\rangle$ , and obtain  $\langle \hat{I}_x(t) \rangle \simeq \delta \mathcal{W}_{\text{SSH}}/\Omega_B$ . Similarly, when  $\Delta\hat{H} = \delta_t \sum_{l, \alpha=e/g} l \hat{n}_{l\alpha}$ , we also have  $\langle \Delta\hat{I}_x(t) \rangle \propto \delta_t$ . In this case,

$$\begin{aligned} &\int_0^t ds \left[ \hat{U}^\dagger(s) \sum_{l, \alpha=e/g} l \hat{n}_{l\alpha} \hat{U}(s), \hat{U}^\dagger(t) \hat{I}_x \hat{U}^\dagger(t) \right] \\ &\equiv S(\Omega_A, \Omega_B, t) \equiv \tilde{S}(\Omega_A, \Omega_B) + \text{osc. term}, \end{aligned} \quad (\text{C4})$$

where  $S(\Omega_A, \Omega_B, t)$ ,  $\tilde{S}(\Omega_A, \Omega_B) \neq 0$  but does not have a direct relation with  $\mathcal{W}_{\text{SSH}}$ . We plot numerically evaluated result for  $S(\Omega_A, \Omega_B, t)$  in Fig. C.1.

### Appendix D: Alternative protocol for the SSH clock spectroscopy

We show in Fig. D.1 an alternative protocol for the SSH clock spectroscopy. In this protocol, we first adiabatically prepare an initial condition  $|0, g\rangle + |-1, e\rangle/\sqrt{2}$ ,

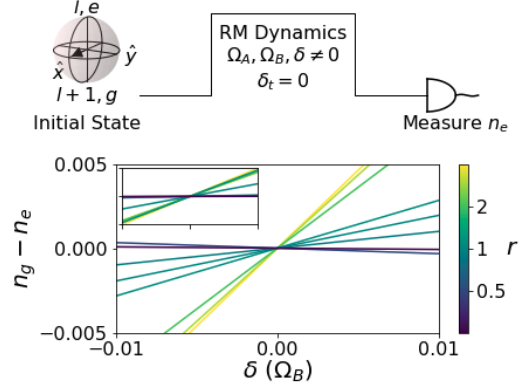


FIG. D.1. Alternative SSH clock spectroscopy. Upper panel: protocol. Lower panel: numerical simulation.

then turn on the RM dynamics for time  $t_B = \pi/\Omega_B$ , followed by measuring  $-S_z$ . In fact, with this protocol, we can analytically obtain  $\langle \hat{S}_z(t) \rangle = -\langle \hat{I}_x(t) \rangle$ , where  $\langle \hat{I}_x \rangle$  is precisely given by the results in Appendix. C.

### Appendix E: AC Stark shift in Wannier-Stark OLCs

The full Hamiltonian in the lab frame, when driving one of the sideband transitions, reads

$$\begin{aligned} \hat{H}_{\text{lab}}^s/\hbar &= \frac{\Omega^s I_0}{2} e^{-\mathbf{i}\omega_1 t} \sum_l \left( e^{\mathbf{i}l\phi} \mathcal{J}_0(\tilde{J}) \hat{c}_{le}^\dagger \hat{c}_{lg} \right. \\ &\quad \left. + e^{\mathbf{i}l\phi} e^{\mathbf{i}(\pi+\phi)/2} \mathcal{J}_{-1}(\tilde{J}) \hat{c}_{le}^\dagger \hat{c}_{l+1g} \right) + \text{h.c.} \end{aligned} \quad (\text{E1})$$

If one goes to the rotating frame of the sideband, without the rotating wave approximation, we get

$$\begin{aligned} \hat{H}_{\text{RF}}^s/\hbar &= \frac{\Omega^s I_0}{2} \sum_l \left( e^{\mathbf{i}l\phi} e^{\mathbf{i}\Delta t} \mathcal{J}_0(\tilde{J}) \hat{c}_{le}^\dagger \hat{c}_{lg} \right. \\ &\quad \left. + e^{\mathbf{i}l\phi} e^{\mathbf{i}(\pi+\phi)/2} \mathcal{J}_{-1}(\tilde{J}) \hat{c}_{le}^\dagger \hat{c}_{l+1g} \right) + \text{h.c.} \end{aligned} \quad (\text{E2})$$

The we go to the rotating-gauge frame where all the couplings are real:

$$\begin{aligned} &\hat{H}_{\text{RF}}^s/\hbar \\ &= \frac{\Omega^s I_0}{2} \sum_l \left( e^{\mathbf{i}\Delta t} \mathcal{J}_0(\tilde{J}) \hat{a}_{le}^\dagger \hat{a}_{lg} + \mathcal{J}_{-1}(\tilde{J}) \hat{a}_{le}^\dagger \hat{a}_{l+1g} \right) + \text{h.c.} \\ &\simeq \frac{\Omega^s I_0 \mathcal{J}_{-1}(\tilde{J})}{2} \sum_l \left( \hat{a}_{le}^\dagger \hat{a}_{l+1g} + \text{h.c.} \right) \\ &\quad - \frac{\left( \Omega^s I_0 \mathcal{J}_0(\tilde{J}) \right)^2}{4\Delta} \sum_l \left( \hat{a}_{lg}^\dagger \hat{a}_{lg} - \hat{a}_{le}^\dagger \hat{a}_{le} \right). \end{aligned} \quad (\text{E3})$$

The last line of the above equation accounts for the AC Stark shift. Similarly, we can repeat the above analysis

for the carrier drive an obtain

$$\begin{aligned}
& \hat{H}_{\text{SSH}}^c/\hbar \\
&= \frac{\Omega^c I_0}{2} \sum_l \left( \mathcal{J}_0(\tilde{J}) \hat{a}_{le}^\dagger \hat{a}_{lg} + e^{-i\Delta t} \mathcal{J}_{-1}(\tilde{J}) \hat{a}_{le}^\dagger \hat{a}_{l+1g} \right) + \text{h.c.} \\
&\simeq \frac{\Omega^c I_0 \mathcal{J}_0(\tilde{J})}{2} \sum_l \left( \hat{a}_{le}^\dagger \hat{a}_{lg} + \text{h.c.} \right) \\
&\quad - \frac{\left( \Omega^c I_0 \mathcal{J}_{-1}(\tilde{J}) \right)^2}{4\Delta} \sum_l \left( \hat{a}_{le}^\dagger \hat{a}_{le} - \hat{a}_{lg}^\dagger \hat{a}_{lg} \right). \quad (\text{E4})
\end{aligned}$$

In the main text, we consider a shallow lattice with lattice depth  $5E_r$ , which gives us  $J_0(\tilde{J})/J_1(\tilde{J}) \simeq 1.73$ .

- 
- [1] T. L. Nicholson, S. L. Campbell, R. B. Hutson, G. E. Marti, B. J. Bloom, R. L. McNally, W. Zhang, M. D. Barrett, M. S. Safronova, G. F. Strouse, W. L. Tew, and J. Ye, “Systematic evaluation of an atomic clock at  $2 \times 10^{-18}$  total uncertainty,” *Nature Communications* **6**, 6896 (2015), arXiv:1412.8261 [physics.atom-ph].
- [2] Andrew D. Ludlow, Martin M. Boyd, Jun Ye, E. Peik, and P. O. Schmidt, “Optical atomic clocks,” *Rev. Mod. Phys.* **87**, 637–701 (2015).
- [3] S. L. Campbell, R. B. Hutson, G. E. Marti, A. Goban, N. Darkwah Oppong, R. L. McNally, L. Sonderhouse, J. M. Robinson, W. Zhang, B. J. Bloom, and J. Ye, “A Fermi-degenerate three-dimensional optical lattice clock,” *Science* **358**, 90–94 (2017), arXiv:1702.01210 [physics.atom-ph].
- [4] W. F. McGrew, X. Zhang, R. J. Fasano, S. A. Schäffer, K. Beloy, D. Nicolodi, R. C. Brown, N. Hinkley, G. Milani, M. Schioppo, T. H. Yoon, and A. D. Ludlow, “Atomic clock performance enabling geodesy below the centimetre level,” *Nature (London)* **564**, 87–90 (2018).
- [5] E. Oelker, R. B. Hutson, C. J. Kennedy, L. Sonderhouse, T. Bothwell, A. Goban, D. Kedar, C. Sanner, J. M. Robinson, G. E. Marti, D. G. Matei, T. Legero, M. Giunta, R. Holzwarth, F. Riehle, U. Sterr, and J. Ye, “Demonstration of  $4.8 \times 10^{-17}$  stability at 1 s for two independent optical clocks,” *Nature Photonics* **13**, 714–719 (2019).
- [6] Tobias Bothwell, Colin J. Kennedy, Alexander Aeppli, Dhruv Kedar, John M. Robinson, Eric Oelker, Alexander Staron, and Jun Ye, “Resolving the gravitational redshift across a millimetre-scale atomic sample,” *Nature* **602**, 420–424 (2022).
- [7] Xin Zheng, Jonathan Dolde, Varun Lochab, Brett N. Merriman, Haoran Li, and Shimon Kolkowitz, “Differential clock comparisons with a multiplexed optical lattice clock,” *Nature (London)* **602**, 425–430 (2022), arXiv:2109.12237 [physics.atom-ph].
- [8] Alexander Aeppli, Anjun Chu, Tobias Bothwell, Colin J. Kennedy, Dhruv Kedar, Peiru He, Ana Maria Rey, and Jun Ye, “Hamiltonian engineering of spin-orbit-coupled fermions in a wannier-stark optical lattice clock,” *Science Advances* **8**, eadc9242 (2022), <https://www.science.org/doi/pdf/10.1126/sciadv.adc9242>.
- [9] Kyle Beloy, Martha I. Bodine, Tobias Bothwell, Samuel M. Brewer, Sarah L. Bromley, Jwo-Sy Chen, Jean-Daniel Deschênes, Scott A. Diddams, Robert J. Fasano, Tara M. Fortier, Youssef S. Hassan, David B. Hume, Dhruv Kedar, Colin J. Kennedy, Isaac Khader, Amanda Koepke, David R. Leibbrandt, Holly Leopardi, Andrew D. Ludlow, William F. McGrew, William R. Milner, Nathan R. Newbury, Daniele Nicolodi, Eric Oelker, Thomas E. Parker, John M. Robinson, Stefania Romisch, Stefan A. Schäffer, Jeffrey A. Sherman, Laura C. Sinclair, Lindsay Sonderhouse, William C. Swann, Jian Yao, Jun Ye, Xiaogang Zhang, and Collaboration Boulder Atomic Clock Optical Network, “Frequency ratio measurements at 18-digit accuracy using an optical clock network,” *Nature* **591**, 564–569 (2021).
- [10] Alexander Aeppli, Kyungtae Kim, William Warfield, Marianna S. Safronova, and Jun Ye, “Clock with  $8 \times 10^{-19}$  systematic uncertainty,” *Phys. Rev. Lett.* **133**, 023401 (2024).
- [11] N. R. Cooper, J. Dalibard, and I. B. Spielman, “Topological bands for ultracold atoms,” *Reviews of Modern Physics* **91**, 015005 (2019), arXiv:1803.00249 [cond-mat.quant-gas].
- [12] W. P. Su, J. R. Schrieffer, and A. J. Heeger, “Solitons in polyacetylene,” *Phys. Rev. Lett.* **42**, 1698–1701 (1979).
- [13] W. P. Su, J. R. Schrieffer, and A. J. Heeger, “Soliton excitations in polyacetylene,” *Phys. Rev. B* **22**, 2099–2111 (1980).
- [14] M. J. Rice and E. J. Mele, “Elementary excitations of a linearly conjugated diatomic polymer,” *Phys. Rev. Lett.* **49**, 1455–1459 (1982).
- [15] Marcos Atala, Monika Aidelsburger, Julio T. Barreiro, Dmitry Abanin, Takuya Kitagawa, Eugene Demler, and Immanuel Bloch, “Direct measurement of the Zak phase in topological Bloch bands,” *Nature Physics* **9**, 795–800 (2013), arXiv:1212.0572 [cond-mat.quant-gas].
- [16] M. Lohse, C. Schweizer, O. Zilberberg, M. Aidelsburger, and I. Bloch, “A Thouless quantum pump with ultracold bosonic atoms in an optical superlattice,” *Nature Physics* **12**, 350–354 (2016), arXiv:1507.02225 [cond-mat.quant-gas].
- [17] Shuta Nakajima, Takafumi Tomita, Shintaro Taie, Tomohiro Ichinose, Hideki Ozawa, Lei Wang, Matthias Troyer,

- and Yoshiro Takahashi, “Topological Thouless pumping of ultracold fermions,” *Nature Physics* **12**, 296–300 (2016), arXiv:1507.02223 [cond-mat.quant-gas].
- [18] Anne-Sophie Walter, Zijie Zhu, Marius Gächter, Joaquín Minguzzi, Stephan Roschinski, Kilian Sandholzer, Konrad Viebahn, and Tilman Esslinger, “Quantization and its breakdown in a hubbard–thouless pump,” *Nature Physics* **19**, 1471–1475 (2023).
- [19] Eric J. Meier, Fangzhao Alex An, and Bryce Gadway, “Observation of the topological soliton state in the Su-Schrieffer-Heeger model,” *Nature Communications* **7**, 13986 (2016), arXiv:1607.02811 [cond-mat.quant-gas].
- [20] Eric J. Meier, Fangzhao Alex An, Alexandre Dauphin, Maria Maffei, Pietro Massignan, Taylor L. Hughes, and Bryce Gadway, “Observation of the topological Anderson insulator in disordered atomic wires,” *Science* **362**, 929–933 (2018), arXiv:1802.02109 [cond-mat.quant-gas].
- [21] Tao Yuan, Chao Zeng, Yi-Yi Mao, Fei-Fei Wu, Yan-Jun Xie, Wen-Zhuo Zhang, Han-Ning Dai, Yu-Ao Chen, and Jian-Wei Pan, “Realizing robust edge-to-edge transport of atomic momentum states in a dynamically modulated synthetic lattice,” *Phys. Rev. Res.* **5**, L032005 (2023).
- [22] Sylvain de Léséleuc, Vincent Lienhard, Pascal Scholl, Daniel Barredo, Sebastian Weber, Nicolai Lang, Hans Peter Büchler, Thierry Lahaye, and Antoine Browaeys, “Observation of a symmetry-protected topological phase of interacting bosons with Rydberg atoms,” *Science* **365**, 775–780 (2019), arXiv:1810.13286 [quant-ph].
- [23] S. K. Kanungo, J. D. Whalen, Y. Lu, M. Yuan, S. Dasgupta, F. B. Dunning, K. R. A. Hazzard, and T. C. Killian, “Realizing topological edge states with Rydberg-atom synthetic dimensions,” *Nature Communications* **13**, 972 (2022), arXiv:2101.02871 [physics.atom-ph].
- [24] Martin Leder, Christopher Grossert, Lukas Sitta, Maximilian Genske, Achim Rosch, and Martin Weitz, “Real-space imaging of a topologically protected edge state with ultracold atoms in an amplitude-chirped optical lattice,” *Nature Communications* **7**, 13112 (2016), arXiv:1604.02060 [cond-mat.quant-gas].
- [25] Or Katz, Lei Feng, Diego Porras, and Christopher Monroe, “Observing topological insulator phases with a programmable quantum simulator,” (2024), arXiv:2401.10362 [quant-ph].
- [26] Dizhou Xie, Wei Gou, Teng Xiao, Bryce Gadway, and Bo Yan, “Topological characterizations of an extended Su-Schrieffer-Heeger model,” *npj Quantum Information* **5**, 55 (2019), arXiv:1906.12019 [cond-mat.quant-gas].
- [27] H.-I. Lu, M. Schemmer, L. M. Ayccock, D. Genkina, S. Sugawa, and I. B. Spielman, “Geometrical pumping with a bose-einstein condensate,” *Phys. Rev. Lett.* **116**, 200402 (2016).
- [28] Cristian D. Panda, Matthew J. Tao, Miguel Ceja, Justin Khoury, Guglielmo M. Tino, and Holger Müller, “Measuring gravitational attraction with a lattice atom interferometer,” *Nature (London)* **631**, 515–520 (2024), arXiv:2310.01344 [physics.atom-ph].
- [29] Pierre Lemonde and Peter Wolf, “Optical lattice clock with atoms confined in a shallow trap,” *Phys. Rev. A* **72**, 033409 (2005).
- [30] Michael L. Wall, Andrew P. Koller, Shuming Li, Xibo Zhang, Nigel R. Cooper, Jun Ye, and Ana Maria Rey, “Synthetic spin-orbit coupling in an optical lattice clock,” *Phys. Rev. Lett.* **116**, 035301 (2016).
- [31] L. F. Livi, G. Cappellini, M. Diem, L. Franchi, C. Clivati, M. Frittelli, F. Levi, D. Calonico, J. Catani, M. Inguscio, and L. Fallani, “Synthetic dimensions and spin-orbit coupling with an optical clock transition,” *Phys. Rev. Lett.* **117**, 220401 (2016).
- [32] S. Kolkowitz, S. L. Bromley, T. Bothwell, M. L. Wall, G. E. Marti, A. P. Koller, X. Zhang, A. M. Rey, and J. Ye, “Spin-orbit-coupled fermions in an optical lattice clock,” *Nature* **542**, 66–70 (2017).
- [33] Shanchao Zhang and Gyu-Boong Jo, “Recent advances in spin-orbit coupled quantum gases,” *Journal of Physics and Chemistry of Solids* **128**, 75–86 (2019), spin-Orbit Coupled Materials.
- [34] Simon Wili, Tilman Esslinger, and Konrad Viebahn, “An accordion superlattice for controlling atom separation in optical potentials,” *New Journal of Physics* **25**, 033037 (2023).
- [35] D. J. Thouless, “Quantization of particle transport,” *Phys. Rev. B* **27**, 6083–6087 (1983).
- [36] Q. Niu and D. J. Thouless, “Quantised adiabatic charge transport in the presence of substrate disorder and many-body interaction,” *Journal of Physics A Mathematical General* **17**, 2453–2462 (1984).
- [37] Di Xiao, Ming-Che Chang, and Qian Niu, “Berry phase effects on electronic properties,” *Reviews of Modern Physics* **82**, 1959–2007 (2010), arXiv:0907.2021 [cond-mat.mes-hall].
- [38] Roberta Citro and Monika Aidelsburger, “Thouless pumping and topology,” *Nature Reviews Physics* **5**, 87–101 (2023), arXiv:2210.02050 [cond-mat.quant-gas].
- [39] Alexander Impertro, Simon Karch, Julian F. Wienand, SeungJung Huh, Christian Schweizer, Immanuel Bloch, and Monika Aidelsburger, “Local readout and control of current and kinetic energy operators in optical lattices,” *Phys. Rev. Lett.* **133**, 063401 (2024).
- [40] M. S. Rudner and L. S. Levitov, “Topological transition in a non-hermitian quantum walk,” *Phys. Rev. Lett.* **102**, 065703 (2009).
- [41] Filippo Cardano, Alessio D’Errico, Alexandre Dauphin, Maria Maffei, Bruno Piccirillo, Corrado de Lisio, Giulio de Filippis, Vittorio Cataudella, Enrico Santamato, Lorenzo Marrucci, Maciej Lewenstein, and Pietro Massignan, “Detection of Zak phases and topological invariants in a chiral quantum walk of twisted photons,” *Nature Communications* **8**, 15516 (2017), arXiv:1610.06322 [cond-mat.mes-hall].
- [42] Maria Maffei, Alexandre Dauphin, Filippo Cardano, Maciej Lewenstein, and Pietro Massignan, “Topological characterization of chiral models through their long time dynamics,” *New Journal of Physics* **20**, 013023 (2018), arXiv:1708.02778 [cond-mat.other].
- [43] R. Wang and Z. Song, “Robustness of the pumping charge to dynamic disorder,” *Phys. Rev. B* **100**, 184304 (2019).
- [44] Bernd Lücke, Jan Peise, Giuseppe Vitagliano, Jan Arlt, Luis Santos, Géza Tóth, and Carsten Klempt, “Detecting Multiparticle Entanglement of Dicke States,” *Phys. Rev. Lett.* **112**, 155304 (2014), arXiv:1403.4542 [quant-ph].
- [45] Lucas Gabardos, Bihui Zhu, Steven Lepoutre, Ana Maria Rey, Bruno Laburthe-Tolra, and Laurent Vernac, “Relaxation of the Collective Magnetization of a Dense 3D Array of Interacting Dipolar  $S = 3$  Atoms,” *Phys. Rev. Lett.* **125**, 143401 (2020), arXiv:2005.13487 [cond-

- mat.quant-gas].
- [46] Achim Peters, Keng Yeow Chung, and Steven Chu, “Measurement of gravitational acceleration by dropping atoms,” *Nature (London)* **400**, 849–852 (1999).
- [47] G. Rosi, F. Sorrentino, L. Cacciapuoti, M. Prevedelli, and G. M. Tino, “Precision measurement of the Newtonian gravitational constant using cold atoms,” *Nature (London)* **510**, 518–521 (2014), arXiv:1412.7954 [physics.atom-ph].
- [48] Achim Peters, Keng Yeow Chung, and Steven Chu, “Measurement of gravitational acceleration by dropping atoms,” *Nature* **400**, 849–852 (1999).
- [49] P. Cladé, S. Guellati-Khélifa, C. Schwob, F. Nez, L. Julien, and F. Biraben, “A promising method for the measurement of the local acceleration of gravity using Bloch oscillations of ultracold atoms in a vertical standing wave,” *EPL (Europhysics Letters)* **71**, 730–736 (2005), arXiv:physics/0506225 [physics.atom-ph].
- [50] Renée Charrière, Malo Cadoret, Nassim Zahzam, Yannick Bidet, and Alexandre Bresson, “Local gravity measurement with the combination of atom interferometry and Bloch oscillations,” *Phys. Rev. A* **85**, 013639 (2012).
- [51] Xian Zhang, Ruben Pablo del Aguila, Tommaso Mazzoni, Nicola Poli, and Guglielmo M. Tino, “Trapped-atom interferometer with ultracold Sr atoms,” *Phys. Rev. A* **94**, 043608 (2016).
- [52] Victoria Xu, Matt Jaffe, Cristian D. Panda, Sofus L. Kristensen, Logan W. Clark, and Holger Müller, “Probing gravity by holding atoms for 20 seconds,” *Science* **366**, 745–749 (2019), arXiv:1907.03054 [physics.atom-ph].
- [53] Cristian D. Panda, Matthew Tao, James Egelhoff, Miguel Ceja, Victoria Xu, and Holger Müller, “Coherence limits in lattice atom interferometry at the one-minute scale,” *Nature Physics* **20**, 1234–1239 (2024).
- [54] Holger Müller, Sheng-wei Chiow, Quan Long, Sven Herrmann, and Steven Chu, “Atom interferometry with up to 24-photon-momentum-transfer beam splitters,” *Phys. Rev. Lett.* **100**, 180405 (2008).
- [55] B. Pelle, A. Hilico, G. Tackmann, Q. Beaufils, and F. Pereira dos Santos, “State-labeling Wannier-Stark atomic interferometers,” *Phys. Rev. A* **87**, 023601 (2013), arXiv:1301.5415 [physics.atom-ph].
- [56] Anjun Chu, Peiru He, James K. Thompson, and Ana Maria Rey, “Quantum enhanced cavity qed interferometer with partially delocalized atoms in lattices,” *Phys. Rev. Lett.* **127**, 210401 (2021).
- [57] Wenjie Liu, Yongguan Ke, and Chaohong Lee, “Shortcuts to adiabatic Thouless pumping,” arXiv e-prints, arXiv:2401.17081 (2024), arXiv:2401.17081 [quant-ph].
- [58] Y.-T. Lin, D. M. Kennes, M. Pletyukhov, C. S. Weber, H. Schoeller, and V. Meden, “Interacting rice-mele model: Bulk and boundaries,” *Phys. Rev. B* **102**, 085122 (2020).
- [59]  $\sum_k \mathcal{J}_{\nu+k}(u) \mathcal{J}_k(u) e^{ik\alpha} = \mathcal{J}_\nu \left( 2u \sin \left( \frac{\alpha}{2} \right) \right) e^{-i\nu(\pi+\alpha)/2}$ .